Journal of Alloys and Compounds 853 (2021) 157298

Contents lists available at ScienceDirect

Journal of Alloys and Compounds

journal homepage: http://www.elsevier.com/locate/jalcom

Effects of nitrogen incorporation on N-doped DLC thin film electrodes fabricated by dielectric barrier discharge plasma: Structural evolution and electrochemical performances

M. Nilkar [a, b], F.E. Ghodsi [a, *], S. Jafari [a], D. Thiry [b], R. Snyders [b, c]

[a] Department of Physics, Faculty of Science, University of Guilan, P.O. Box 413351914, Rasht, Iran
[b] Chimie des Interactions Plasma-Surface(ChIPS), CIRMAP, Université de Mons, 23 Place du Parc, 7000 Mons, Belgium
[c] Materia Nova Research Center, Parc Initialis, Avenue Nicolas Copernic 1, B-7000, Mons, Belgium

ARTICLE INFO

Article history:
Received 4 August 2020
Received in revised form
18 September 2020
Accepted 21 September 2020
Available online 22 September 2020

Keywords:
Nitrogen-doped DLC thin film
Structural
Optical and electrochemical properties
Dielectric barrier discharge plasma

ABSTRACT

Hydrogenated amorphous carbon-nitride (a-C:H:N) thin films (or N-DLC) were deposited on glass and FTO substrates by a dielectric barrier discharge plasma technique using CH_4/N_2 gas mixture. The XPS results reveal that as the nitrogen ratio in the CH_4:N_2 gas mixture increases from 50% to 80%, the nitrogen doping level increased from 5.5 at.% to a maximum value of 11.5 at.% with especially high amounts of pyridinic (6.4 at %), and graphitic (4.7 at %) nitrogen. FEG-SEM results indicate a worm-like porous morphology for the 20%:80% CH_4:N_2 sample, relying on high amounts of pyridinic and graphitic N, which is a favorable structure to boost the ions diffusion process. This optimized N-DLC electrode with high nitrogen incorporation not only exhibits a nearly electrochemical reversibility with ΔE_p (125 mV) and J_{pa}/J_{pc} (1.03) in $K_3Fe(CN)_6$ electrolyte, but also a fast charge transfer constant (6.59×10^{-4} cms^{-1}). The excellent performance of this electrode is ascribed to the high nitrogen doping level, large surface area, the abundant holes, and the high nano-pore volume possessing excellent electron transfer ability for redox reaction. N-DLC thin film exhibits a promising prospect for biosensors and electrochemical electrode applications.

1. Introduction

Recently, carbon-based electrode materials such as diamond-like carbon (DLC) films and boron-doped diamond (BDD) films come to be promising candidates for novel electrochemical electrodes [1–3] and biosensors [4,5]. Among them, BDD thin film as a desirable electrode material exhibits distinguished electrochemical properties [6,7]. However, the fabrication of BDD films requires to high temperatures (about 800 °C) and surface oxidation easily occurs in these films, which decreases the charge transfer rates. Moreover, only few substrates can be used for the deposition of these films [6]. Hence, these problems restrict the application of BDD electrodes and consequently there is still impetus to find a desirable alternative carbon electrode based-material. In this regard, nitrogen-doped hydrogenated amorphous carbon (a-C:H:N) electrode, as a modified DLC electrode, presents a promising alternative to extremely high cost BDD electrode due to its similar electrochemical properties such as wide potential window, low background current, and high stability for electrochemical reaction [4,6,8]. Furthermore, in contrast to BDD films, the a-C:H:N films can be deposited on diverse substrates at room temperature for lower production costs [9].

Nitrogen doping in DLC electrodes boosts the electrical conductivity of the electrode by narrowing the band gap, which leads to enhancing the electrochemical activity of the electrode material [8]. In fact, exciting the excess electrons in the a-C:H:N electrodes promotes the incorporation of graphitic N–C which can lead to a significant increase in the conductivity [10]. Besides, pyridinic N and pyrrolic N provided from nitrogen doping can develop the formation of large amounts of nanopores [10,11] and supply large electrode/electrolyte interfaces for the fast charge-transfer reaction, which leads to an enhanced electrochemical efficiency [10]. a-C:H:N films are already known as a desirable electro-analytical performance, e.g., voltammetry analysis for heavy metals detection [8,12], and organic analytes detection such as glucose, dopamine and DNA [13,14]. Furthermore, the a-C:H:N thin film can also

* Corresponding author.
E-mail address: feghodsi@guilan.ac.ir (F.E. Ghodsi).

https://doi.org/10.1016/j.jallcom.2020.157298
0925-8388/

be employed as anti-reflective coatings in IR sensors [15] because of its high chemical stability and low reflectance in the IR region. The idea of employing a-C:H:N thin films in solar cells as an IR transparent coating emanates as an impressive option for future optoelectronic devices [16]. From the aforementioned explanations, it can be concluded that by tuning the nitrogen doping level, the electrochemical performance and optical band gap of a-C:H:N films can be well improved.

Among many techniques that can be utilized for the a-C:H:N thin films fabrication (such as chemical vapor deposition [17], magnetron sputtering [18], pulsed laser deposition [19], cathodic arc deposition [20] etc.), extensive developments are being placed on the non-thermal plasma-based processes [8,21,22]. Non-thermal plasma deposition processes offer some advantages over the typical aforementioned processes. Firstly, it provides high efficiency of surface activation by free-radicals and charged particles (especially ions) in the plasma medium [21,23,24]. Second, due to good adhesion to the substrate in the deposition process at ambient temperature, the non-thermal plasmas are very attractive for deposition on thermo-sensitive materials [25]. In this regard, Dielectric Barrier Discharge (DBD) plasma technique can provide approximately high density of chemical functionalities and active species in both streamer and silent modes as a low cost non-thermal plasma generation technique [22,26]. To fabricate a N-doped DLC electrode (or a-C:H:N film) by a DBD plasma with hydrocarbon/nitrogen gas mixture, the presence of high electronegative nitrogen ions in the plasma medium is very useful to produce the pyridinic N-sites, generating high active sites in a-C:H:N films [27,28]. The electrochemical performance of the N-doped DLC films could be eventually adjusted by these sites.

In the past decade, some research groups attempted to fabricate a-C:H:N or N-DLC films to develop new electrode materials achieving desirable voltammetric characteristics. Zhou et al. [8] reported the effect of nitrogen content on the electrochemical properties and microstructure attributes of N-DLC films synthesized by plasma-enhanced CVD (PECVD). They found that a negative bias voltage of −550 V, the N-DLC electrode exhibits a nearly reversible electrode reaction by ΔE_p at 209 mV and I_p^{ox}/I_p^{red} at 0.88 in $K_3Fe(CN)_6$ solution. Besides, for this bias a high C-N bond concentration of 5.4% was achieved. Zhang et al. [11] investigated the microstructure variation of N-doped amorphous carbon films fabricated by magnetron sputtering of carbon target at the different negative bias voltages in argon and nitrogen atmospheres. They found that higher value of negative bias (150 V) can enforce the generation of nanoporous structures explained by ion etching effect. As an important result, they found that high-energy N ions bombardment restricts the nitrogen content and consequently the deposition rate in CN-species.

Niu et al. [29] investigated the structural and morphological properties of a-C:H:N films deposited by DBD-plasma in low discharge pressures by different hydrocarbons. They showed that raising the discharge pressure gives rise to growing in the film's surface roughness and deposition rate. Moreover, the properties of deposited polymer-like films could turn into diamond-like when the discharge pressure was increased. However, there is no report on a-C:H:N (or N-DLC) thin films as an electrode material and an anti-reflective coating in IR region fabricated by DBD plasma technique. In addition, the correlation between the structural, optical and electrochemical properties of a-C:H:N thin films based on this fascinating low-cost plasma method has not been reported, yet.

In the present work, a-C:H:N thin films have been successfully deposited on glass and FTO substrates in a homogenous silent and streamer-like non-thermal plasma using a CH_4/N_2 gas mixture by DBD. The influence of nitrogen concentration on the structural, optical, and electrochemical properties as well as microstructure evolution of the a-C:H:N were investigated. An additional motivation of this work is the investigation of the possible use of these samples as an IR anti-reflective coating candidate which indicate a good transparency associated with low reflectance (<0.02) in IR region. In this manuscript, we focused on the electrode activities of the samples by increasing the nitrogen content. Moreover, correlations between the structural and morphological properties with electrochemical performances were discussed.

2. Experimental details

2.1. Film preparation

The a-C:H:N thin films were fabricated by DBD plasma technique using a CH_4/N_2 gas mixture on the Corning glass and FTO (fluorine doped tin oxide) substrates for analytical, optical and electrochemical testing, respectively. Before setting the substrates into the vacuum chamber, they were cleaned ultrasonically in a blend of deionized water and ethanol for 15 min, then dried with nitrogen gas flow after rinsing with deionized water.

The DBD plasma chamber is made of stainless steel, and the chamber volume is about 6200 cm^3. The two electrodes in the DBD are made of stainless steel plate with a diameter of 8 cm and thickness 2 cm. As a result, the area of each electrode is 50.2 cm^2. The gap between the two electrodes was regulating to 8 mm. The upper electrode is connected to a high-voltage power supply (20 kV peak-to-peak), while the lower electrode is grounded. Both electrodes are covered by quartz dielectrics ($\varepsilon \approx 4.5$). The substrate was placed on the lower electrode. Before each plasma deposition, the chamber is pumped down by a two-stage rotary vacuum pump to a pressure of 10^{-3} mbar, and then it is filled by the CH_4/N_2 gas mixture to 200 mbar pressure to ensure high gas purity for the discharge. After filling the chamber with the gas mixture, the gases flow was switched off and then the plasma ignited for the deposition process. The experiments were performed for 50%:50%, 40%:60%, 30%:70% and 20%:80% CH_4:N_2 gas ratios. The deposition conditions are introduced in Table 1. A schematic representation of the DBD plasma device as well as the generated plasma in different gas ratios are shown in Fig. 1.

2.2. Characterization

Raman spectra of the deposited N-DLC films were measured by Micro-Raman spectrometer (Takram P50CoR10, Teksan) with a laser excitation wavelength at 532 nm. The Raman spectra were then fitted using both Guassian and Lorentzian functions by OriginPro 9.30 software to evaluate required parameters. To studying the functional groups of the specimens, ATR-FTIR spectra were recorded via a Jasco FTIR-4700 spectrometer with a resolution of 4 cm^{-1}. Besides, PHI 5000 VersaProbe apparatus was utilized for XPS measurements in order to the chemical composition analysis of the a-C:H:N films. A monochromatized Al Kα line (1486.6 eV) was operated as an incident photon source located at 54.7° with respect

Table 1
Discharge conditions of plasma deposition of a-C:H:N thin films.

Discharge Parameter	value
Frequency of power supply	20 KHz
Discharge power	140 W
Discharge pressure	200 mbar
Deposition time	40 min
Discharge gap	8 mm
Operating gases	CH_4+N_2
Substrates	Corning Glass and FTO

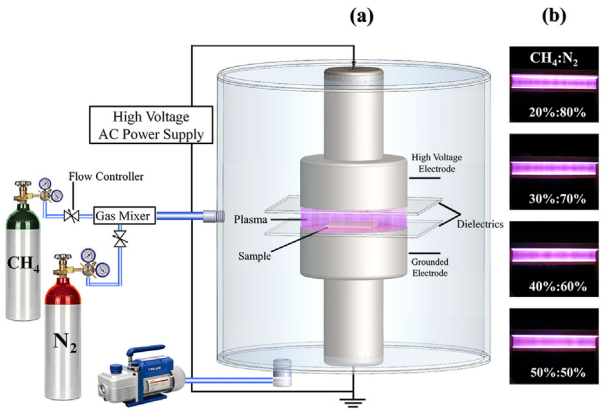

Fig. 1. a) Schematic diagram of the DBD plasma set-up used for the N-DLC thin films deposition. b) Photographs of the plasma medium generated in the DBD reactor for different CH_4:N_2 gas ratios.

to the analyzer axis. Photoelectron spectrum was accumulated at the take-off angle of 45° with respect to the surface normal. The energy analyzer was worked at the constant analyzer energy mode. All spectra were charge-corrected regarding to the hydrocarbon constituent of the C1s peak at 285 eV. The XPS survey was acquired using a pass energy of 117.4 eV. Moreover, pass energy of 23.5 eV was employed according to the high-resolution peaks of each element. The PHI Multipak Software was used concerning to the spectral curve fitting. A Gauss-Lorentz function and a full width at half maximum of 1–1.5 eV were applied. The thicknesses of the films and their surface morphology were analyzed by a field-emission scanning electron microscope (FEG-SEM, MIRA3 TESCAN) operating at 15 kV. Optical transmittance and reflectance of the N-DLC films were measured by employing UV–Vis–NIR spectrophotometer (Cary 5000). The electrochemical measurements were performed in an aqueous solution of 1 M KCl containing 10 mM $K_3Fe(CN)_6$ using an Autolab PGSTAT 30 electrochemical analyzer in a three-electrode system, where the synthesized electrode, Ag/AgCl and platinum plate were served as the working, counter and reference electrodes, respectively. The electrochemical impedance spectroscopy (EIS) measurement was performed using the same system in frequency range of 0.01–105 Hz and at open circuit potential and ac amplitude of 10 mV. Using the Zview software, the impedance spectra were fitted with the equivalent circuit.

3. Results and discussion

3.1. Structural and compositional properties

Raman spectroscopy, as a non-destructive method, is employed to extract the structural information and the presence of defects in a-C:H:N films. Raman spectra of the a-C:H:N thin films with different nitrogen incorporation (in the CH_4:N_2 gas mixture) are exhibited in Fig. 2a.

For all samples, the Raman spectra are dominated by two common features in disorder carbon films recognized as G- and D bands in the region between 1000 and 1800 cm^{-1} and corresponding the second order bands. Due to the bond stretching of all pairs of sp^2, the G peak around 1580-1590 cm^{-1} is raised, while the D peak around 1380-1390 cm^{-1} is owing to the in-plane breathing vibrations of sp^2 carbon atoms in rings. To obtain the parameters of interest, the Raman spectra were deconvoluted using fitting method by Gaussian and Lorentzian functions [30–32]. In addition to the G- and D bands, the first- order Raman spectra exhibits a sub-band approximately around 1520 cm^{-1} named as G1 which can be attributed to fine structures of the sp^2 sites in the amorphous carbon [30,33]. As can be seen from Fig. 2a, because of increasing the finite size of crystallites and the following enhance of the defects density, the intensity of this peak increases when N_2 incorporation enriched [33]. The variation in the G-peak position, intensity ratio of D and G band (i.e., I_D/I_G) as well as full width at half maximum (FWHM) of G-band for the samples are reported in Table 2. With increasing the nitrogen incorporation in the films, an upshift of the G-peak position is observed which refers to the promotion of the clustering associated with evident rising of I_D/I_G [12].

In fact, the increase in the I_D/I_G ratio could be assigned to the increase in the size and number of the sp^2 carbon clusters and consequently the higher existence of complete sp^2 graphitized rings [8,30,34]. In addition, the G-FWHM is related to structural disorder caused by bond angle and bond length distortions. As a result, the lowest G-FWHM value of samples having the most nitrogen content may rely on increasing the graphitization structure [30,31,35].

Another significant parameter which can be obtained from the visible Raman analysis is the grain size of the graphite which is attributed to the in-plane correlation length L_a [30,36]. According to the empirical equation proposed by Robertson [37], the I_D/I_G ratio could be used to estimate the size of the sp^2 clusters, which is described as follows [30,36]:

$$\frac{I_D}{I_G} = C'(\lambda) L_a^2 \quad (1)$$

where L_a is the diameter of a cluster, λ denotes the excitation wavelength (532 nm in this work), and $C'(\lambda)$ is the variable scaling coefficient that is taken as 0.55 nm^{-2} [30,36]. This estimated typical size of graphite clusters increases with decreasing G-FWHM and vice versa. The values of the calculated L_a have been reported in Table 2. In this table, it can be seen that sample 20%:80% presents the highest L_a parameter suggesting the presence of a high level of sp^2 structures which could be explained by its high nitrogen content [30,31,37]. Moreover, the broad asymmetrical and nearly featureless Raman band observed in the high-frequency region (2500-3200 cm^{-1}) is attributed to the D and G second order structures. This broaden second order Raman spectrum observed in defective graphitic carbon materials induced by nitrogen incorporation could be due to the very small size of graphitic crystallites [33,35,38].

In order to deconvolute the 2D region into its possible consistent peaks, this region is compared in Fig. 2b, separately. The most prominent bands named as 2D, D + G1, D + G and 2G, respectively, are demonstrated in the Fig. 2b. The two merging second-order peaks around 2822 and 2926 cm^{-1}, which are common in all samples, are a combination of the D band with the G1 and G band frequency, respectively [39,40]. Another two peaks around 2665 and 3129 cm^{-1} are attributed to the overtone mode of the D band (namely 2D) and G band (namely 2G) since the frequency of these peaks are close to twice that of the D band and G band frequency, respectively [35,39,40]. The small graphitic crystallite size derived from the second order of the Raman spectra is in consistent well with first order of Raman spectra (see Table 2).

Fig. 3a shows ATR-FTIR spectra of specimens with different nitrogen fractions. The transmission spectrum of the samples can be analyzed by considering several typical spectral regions. The broad band at 3700-3100 cm^{-1} is due to the stretching vibrations of O–H and N–H functional groups [29,41–43]. More precisely, this broad peak indicates the presence of the anti-symmetric and symmetric stretching bands of NH2 around 3360 and 3200 cm^{-1}, respectively. It is also observed that more incorporation of N_2 in CH_4/N_2 ratio leads to an increase of the intensity of these bands which can be

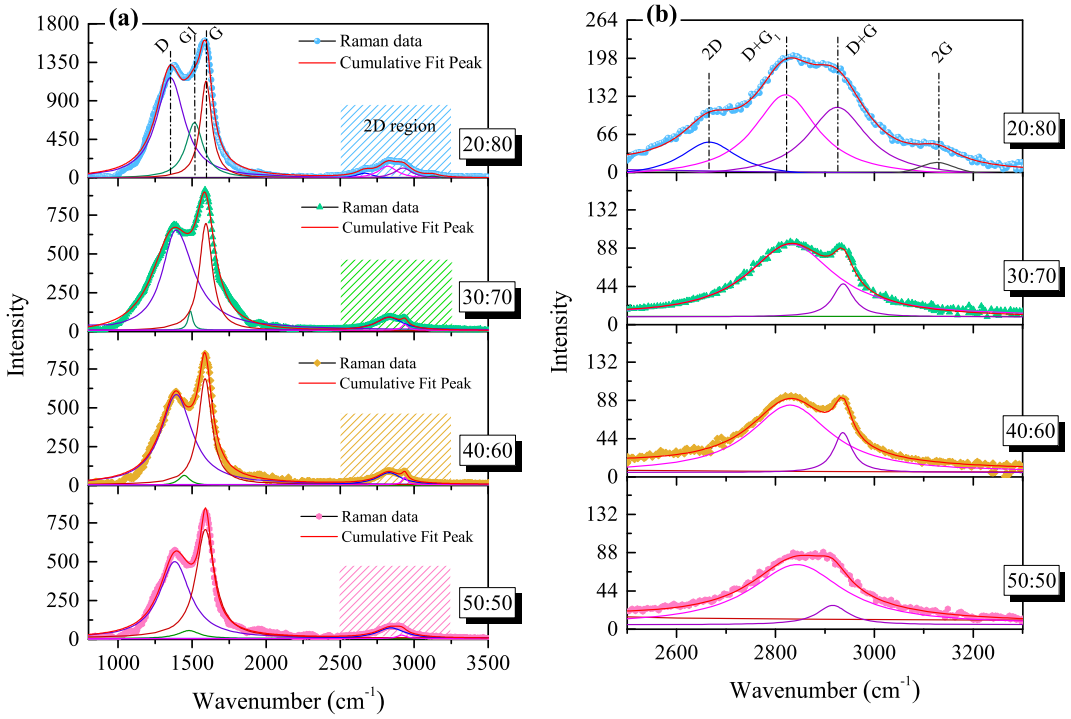

Fig. 2. a) First and second-order Raman spectra of a-C:H:N thin films fabricated at different CH_4:N_2 gas ratios (vs. %), b) Deconvolutions of the second order Raman spectrum.

Table 2
Variation in the I_D/I_G ratio, G-FWHM, G-peak position, graphite cluster size L_a, and optical band gap of the investigated a-C:H:N samples for different CH_4:N_2 gas ratios (vs. %).

CH_4:N_2	I_D/I_G	G-peak position (cm^{-1})	G-FWHM	L_a (nm)	E_g (eV)
50:50	0.72	1587	123	1.15	1.33
40:60	0.85	1589	111	1.24	1.21
30:70	0.92	1592	105	1.30	1.17
20:80	1.03	1596	93	1.37	1.09

attributed to an increase in the N-content of the deposited films. The band observed at 2223 cm^{-1} is attributed to C≡N triple bond stretching vibration which becomes stronger when increasing nitrogen concentration. Similar trend was reported by different authors [29,42]. The band around 1715 cm^{-1} corresponds to a contamination of the carbon films by oxygen [30]. In addition to the observed IR active bands, the D and G bands are detected at 1368 and 1602 cm^{-1}, respectively. The appearance of these features is due to the symmetry breaking in the sp^2 domains caused by the N incorporation into the films which makes these features active in IR spectroscopy [35,41,43]. As can be seen in Fig. 3b, a satisfactory correspondence between ATR-FTIR spectra and the structures observed in the Raman spectra is found. Finally, an apparently increasing activity of the wagging mode of C and N atoms at 832 cm^{-1} as well as wagging mode of H atoms in the N-H group at 609 cm^{-1} is observed with increasing the nitrogen incorporation [44]. The results extracted from ATR-FTIR analysis are also corroborated by Raman spectroscopy.

To elucidate the chemistry of the films, N-DLC films were also investigated by XPS analysis. The hydrocarbon component of the C1s peak at 285 eV was considered as a reference to calibrate the binding energy [45]. The survey spectra of a-C:H:N thin films with different nitrogen contents which includes C, N, and O without any other impurities is presented in Fig. 4. As it is obvious, adding the nitrogen fraction in the feed gas results in a gradual enhance of the intensity of N peak.

To recognize the bonding state of the N-doped DLC films, the

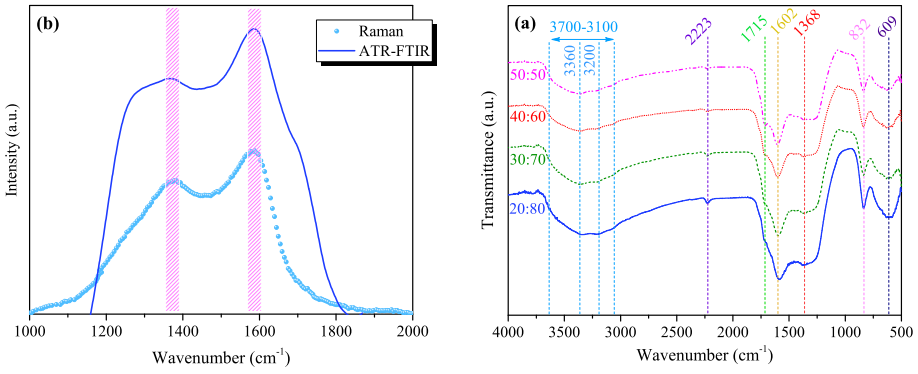

Fig. 3. a) ATR-FTIR transmittance spectra of a-C:H:N samples for different CH_4:N_2 gas ratios (vs. %), b) the IR and Raman spectra relative to sample 20%:80% CH_4:N_2.

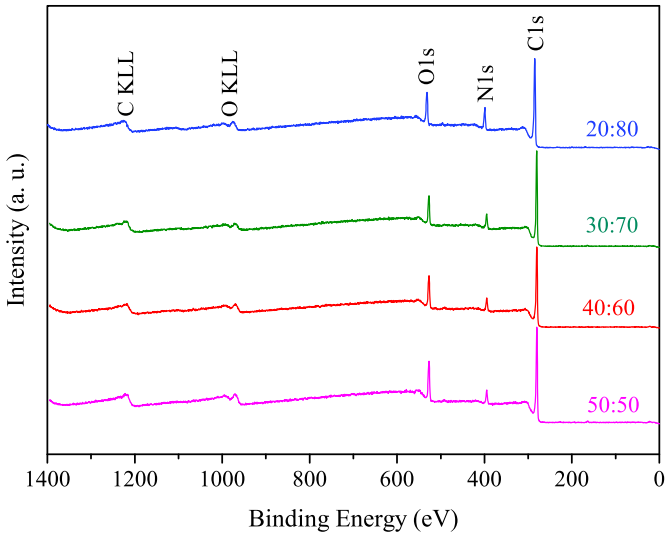

Fig. 4. XPS spectra of a-C:H:N thin films in dependence on the different CH_4:N_2 gas ratios (vs. %).

high-resolution XPS C1s and N1s core level spectra were evaluated, separately (see Fig. 5 and Fig. 6). The high-resolution C1s is fitted by four components corresponding to different bonding states of the carbon atoms. The first component C1 at 284.9 eV is attributed to sp^3/sp^2 C–CR/C=CR (R: H or C), the second one C2 at 285.8 eV is assigned to C–NR/C=NR (R: H or C), the third one C3 at 286.7 eV is ascribed to C≡N, and forth one C4 at 288.2 eV is corresponded to C=O/N–C=O/N–C–O bonds [11,45,46]. The N1s spectra were also deconvoluted into three sub-peaks as shown in Fig. 6. The peak N1 at 399.2 eV is attributed to pyridinic N, N_2 at 400.4 eV is assigned to graphitic N, and N3 at 402.3 eV is corresponded to N–O groups [10,11].

The effect of the nitrogen content on the distribution of the three nitrogen components N1 to N3 in the films are summarized in Table 3. With increasing the nitrogen ratio in the gas mixture from 50% to 80%, the corresponding nitrogen doping level increases from 5.5 at.% to a maximum value of 11.5 at.%. This high nitrogen doping concentration is much more important than that of N-DLC or a-C:H:N electrodes deposited by PECVD technique [6,8], and corresponds to high nitrogen doping level 11.7 at.% obtained by Guo et al. [10], for nitrogen-doped amorphous carbon synthesized through thermal decomposition.

The effect of the nitrogen content on the structure evolution of specimens exhibited a greater amount of pyridinic N, 6.4 at.%, and graphitic N, 4.7 at.%, in the sample 20%:80% relative to the others. This effect provides more nanopores/active sites as well as excess electrons which leads to enhance the electrochemical performance [10]. These results are in accordance with FEG-SEM and EIS outcomes. More details will be brought in the next parts.

3.2. Optical properties

The transmittance and reflectance spectra of a-C:H:N thin films with different nitrogen incorporations as a function of wavelength in the UV–Visible–NIR range (300–2600 nm) are illustrated in Fig. 7. The occurrence of interference fringes in all samples' spectra (transmittance and reflectance) could be due to both homogeneous deposition of the films and desirable thickness. Moreover, good transparency associated with low reflectance (<0.02) in IR region makes a-C:H:N thin films as a proper anti-reflective coating candidate in IR devices [47–49]. Another important aspect of transmittance spectra is concerned with a redshift in band edge with increasing of nitrogen concentration which will be discussed below.

To compute the indirect band gap (E_g) of the specimens, the optical absorption coefficient (α), near the absorption edge, could be obtained by the following equation [50]:

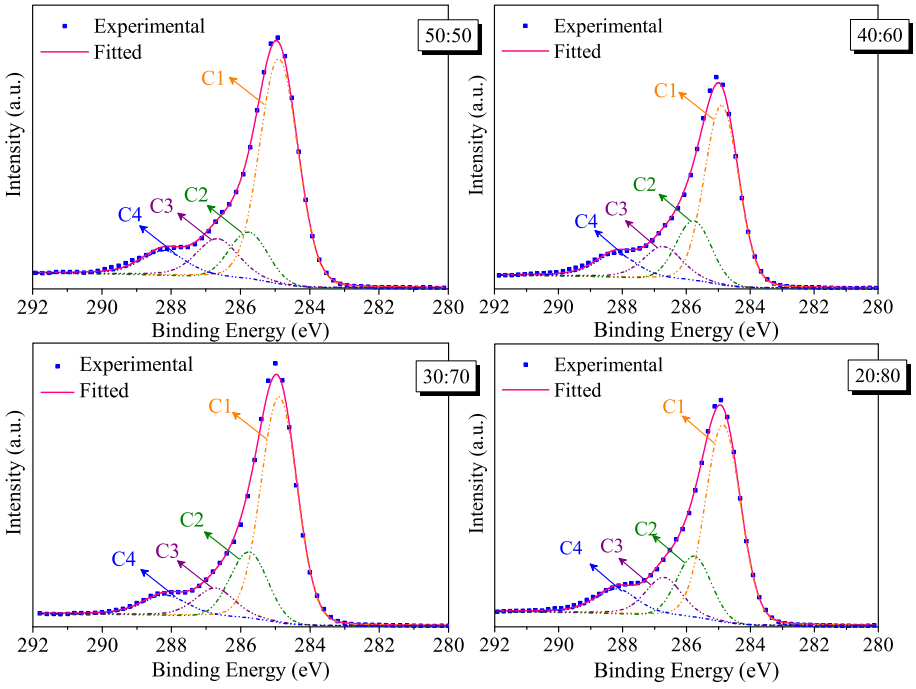

Fig. 5. XPS C1s core spectra of the a-C:H:N thin films deposited at different CH_4:N_2 gas ratios (vs. %).

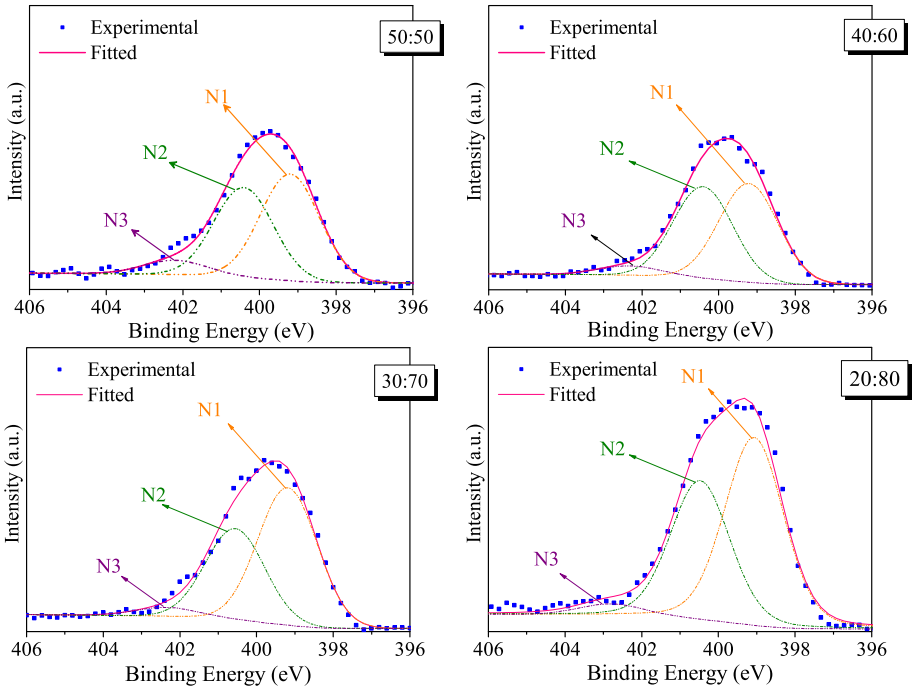

Fig. 6. XPS N1s core spectra of the a-C:H:N thin films deposited at different CH_4:N_2 gas ratios (vs. %).

Table 3
Surface chemical composition of a-C:H:N thin films deposited at different CH_4/N_2 compositions. Data are reported in atom percent, as recorded by XPS. The chemical states of nitrogen are expressed of the total nitrogen normalized to 100%.

CH_4:N_2 gas ratio (%)	Element (at. %)			N/C	Content ratio (%) in sample to fraction of total N (at. %)		
	C	N	O		Pyridinic N	Graphitic N	N-Oxide
50:50	79.9	5.5	14.6	0.07	2.8	2.3	0.4
40:60	79.4	7.1	13.5	0.09	3.5	3.3	0.3
30:70	80.5	8.4	11.1	0.10	4.9	3.3	o.3
20:80	77.0	11.5	11.5	0.15	6.4	4.7	0.4

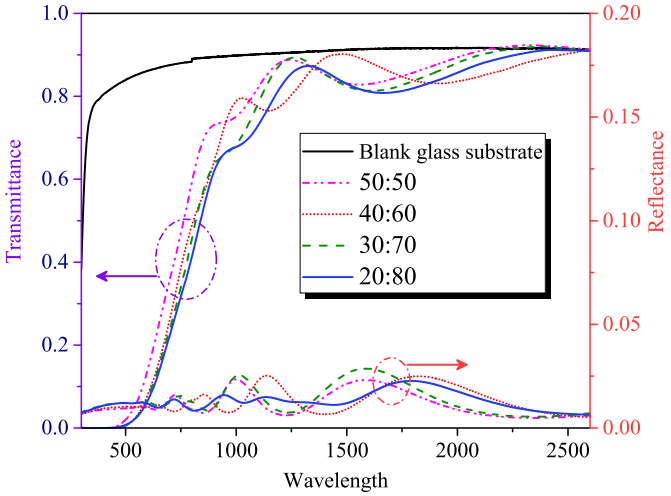

Fig. 7. Optical transmittance and reflectance of the a-C:H:N thin films deposited at different CH_4:N_2 gas ratios (vs. %).

$$\alpha = \frac{1}{d}\ln\left[\frac{(1-R)^2}{2T} + \sqrt{\frac{(1-R)^4}{4T^2} + R^2}\right] \quad (2)$$

in which d denotes the thickness of the film, R and T are the reflectance and transmittance, respectively. The optical band gap of the films was calculated using Tauc's relation:

$$\alpha h\nu = A\left(h\nu - E_g\right)^2 \quad (3)$$

in which hν is the photon energy, A is a constant, and E_g defines the band gap energy. From extrapolating of the linear part of $(\alpha h\nu)^{1/2}$ versus photon energy, the band gap of the N-doped DLC films was specified (see Fig. 8). The achieved results are given in Table 2. It can be learned that the increase in the nitrogen content (in CH_4:N_2 mixture) from 50% to 80% leads to a gradual decrease in optical band gap from 1.33 eV to 1.09 eV.

It is known that due to the π/π^* transitions in sp^2 domains, sp^2 fraction adjusts the optical band gap in all types of amorphous carbon films [51]. Based on the Raman results, increasing nitrogen incorporation leads to an increase in sp^2/sp^3 ratio as well as the increase of sp^2 cluster size. Thereby, the detected redshift can be due to the π states of sp^2 phase which lies near Fermi level and thus it controls the optoelectronic properties [48]. These results indicate that the band gap of N-doped DLC films can be modified by tuning

the feeding amount of nitrogen in these films. Therefore, to reach a narrower band gap with distinguished charge mobility, high nitrogen incorporation must be applied in the gas mixture which provides an easier electron transfer.

3.3. Morphological property

Surface and cross-section FEG-SEM micrographs of the a-C:H:N thin films are given in Fig. 9 for various nitrogen incorporations in CH_4:N_2 gas ratio. As seen in Fig. 9a, the specimen deposited at 50%:50% CH_4:N_2 ratio shows a smooth surface with several spherical grains disseminated on the surface. Increasing the nitrogen concentration to 60% in CH_4:N_2 ratio leads to conglomeration of these small grains and formation of graphite like nanosheets in amorphous a-C:H:N matrix. With raising the nitrogen content up to 70%, the coagulation of the grains becomes more noticeable and the nanosheets become larger. In fact, such structures are associated with graphite nanosheets, carbon nanosheets and solid plates [10,33,52,53].

As discussed before, the existence of the nano-graphite clusters were confirmed from the first- and second-order Raman results. Moreover, pyridinic- and graphitic-N structures can be derived from XPS measurements. According to these structural results, it can be inferred that the formed structures on the surface of thin films may be associated with the carbon nanosheets. Besides, from Fig. 9 (b2) and (c2), it is clear that the carbon nanosheets observed in the a-C:H:N amorphous matrix have a twisted petal-like morphology. Similar morphology for carbon nanosheets has been reported in various literatures based on glow discharge and PECVD techniques and thermal decomposition method [10,54,55]. With increasing the nitrogen concentration to 80% in CH_4:N_2 ratio, the morphology of the a-C:H:N film dramatically changed which is shown in Fig. 9 (d). At a glance, the 20%:80% CH_4:N_2 sample shows a homogeneous dense structure composed of nano-groove and small hole on the upper surface. As is visible in Fig. 1b, when the nitrogen concentration increased from 50% to 80% in the discharge region, the plasma medium changed from silent to a uniform strong streamer mode of plasma achieved. By increasing nitrogen content to 80%, provides numerous avalanches of charged particles including both electrons and ions of the plasma medium. These particles in the streamers can strike to the film surface, make the holes in the upper surface and modify the film morphology and its structure in the deposition process. Moreover, high-magnified image of the hole on the film surface allows us to investigate deeper inside the surface morphology.

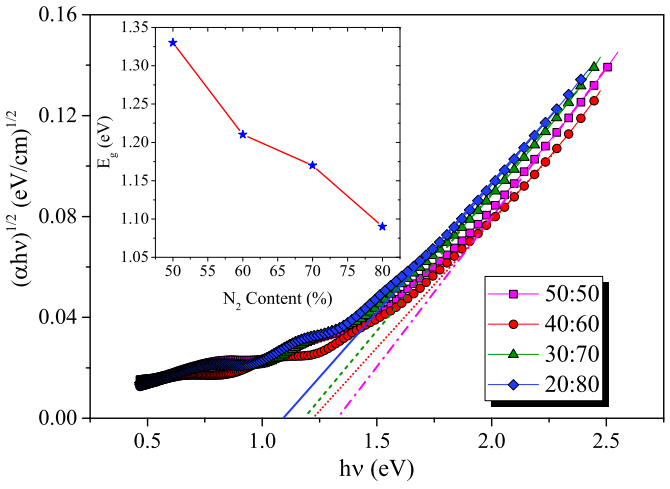

Fig. 8. Tauc plots of the a-C:H:N thin films deposited at different CH_4:N_2 gas ratios (vs. %). The inset shows the band gap energy variation with respect to N_2 content.

As can be seen in Fig. 9 (d2), a worm-like porous morphology is created in the holes on the film surface which is a favorable structure to boost the ions diffusion process. Furthermore, this particular porous structure is depending on high amounts of pyridinic N as well as graphitic N, which is provided in a high nitrogen doping. Indeed, pyridinic N promotes the formation of nanopores, while graphitic N generates excess electrons and enhances the electronic conductivity [10].

Consequently, these promising characteristics, which are exhibited by the DBD plasma deposition technique, can noticeably improve the electrochemical performance of the electrodes. Zhang et al. [11], reported the same morphology obtained by magnetron sputtering technique but with a deteriorated nitrogen doping which is attributed to etching process by high-energy N ions. In the plasma-based deposition techniques, the energy rate of N-ions bombardment plays a major role in CN_x film growth. It was found that the bombardment with low-energy particles could effectively facilitate the film growth.

On the other hand, the bombardment with high-energy particles provides porous morphology with the cost of both deposition rate loss in CN_x films and low nitrogen content [11,56]. In contrast, we found that with employing a CH_4:N_2 DBD plasma, a porous morphology in the a-C:H:N films is originated with high nitrogen content which is favorable for electrochemical electrode applications.

FEG-SEM cross-sectional micrographs were also examined to characterize the films thickness and specially confirming the porous-like morphology in depth of N-DLC films. From Fig. 9 (d3), it can be clearly observed that increasing nitrogen content up to 80% in CH_4:N_2 plasma mixture leads to high level of porosity in a-C:H:N thin films.

3.4. Electrochemical behaviors

Fig. 10 demonstrates cyclic voltammograms (CV) of a-C:H:N electrodes deposited on FTO substrates with different nitrogen concentrations in redox couples of $Fe(CN)_6^{3-/4-}$ measured at different scan rates (5-200 mVs^{-1}). As can be seen from Fig. 10, symmetric CV curves are obtained for different a-C:H:N electrodes which presents a pair of well-defined redox peaks in the all scan rates. Besides, it was found that with the increase of sweep rate, although the shape of CV curves for all electrodes stays unchanged, but the largest CV enclosed area is created for 20%:80% a-C:H:N electrode. This occurrence indicates fast redox reactions at electrode/electrolyte interface and outstanding rate capability for 20%:80% electrode in comparison to others [57].

Furthermore, to evaluate the effect of nitrogen incorporation ratio on the peak current densities of anodic and cathodic reactions, voltammetry profiles of the electrodes are compared at 20 mVs^{-1}, in Fig. 11. It can be seen from Fig. 11 that the a-C:H:N electrode deposited at most nitrogen ratio acquires an outstanding electrochemical performance, since the redox current for this electrode (i.e., sample 20%:80%) is appreciably more than the other electrodes. This behavior in the electrode 20%:80% can refer to both the most amounts of active C-N bonds measured by XPS measurements and nanoporous morphology, which leads to an enhanced electrochemical performance due to raising the current respond [8,58,59].

Moreover, in order to investigate the reversibility of the redox reaction, the difference between the reduction and oxidation peak potentials (ΔE_p) likewise the anodic and cathodic peak current density ratio (J_{pa}/J_{pc}) is calculated at scan rate of 20 mVs-1. The outcomes outputs are given in Table 4. It was found that ΔE_p and J_{pa}/

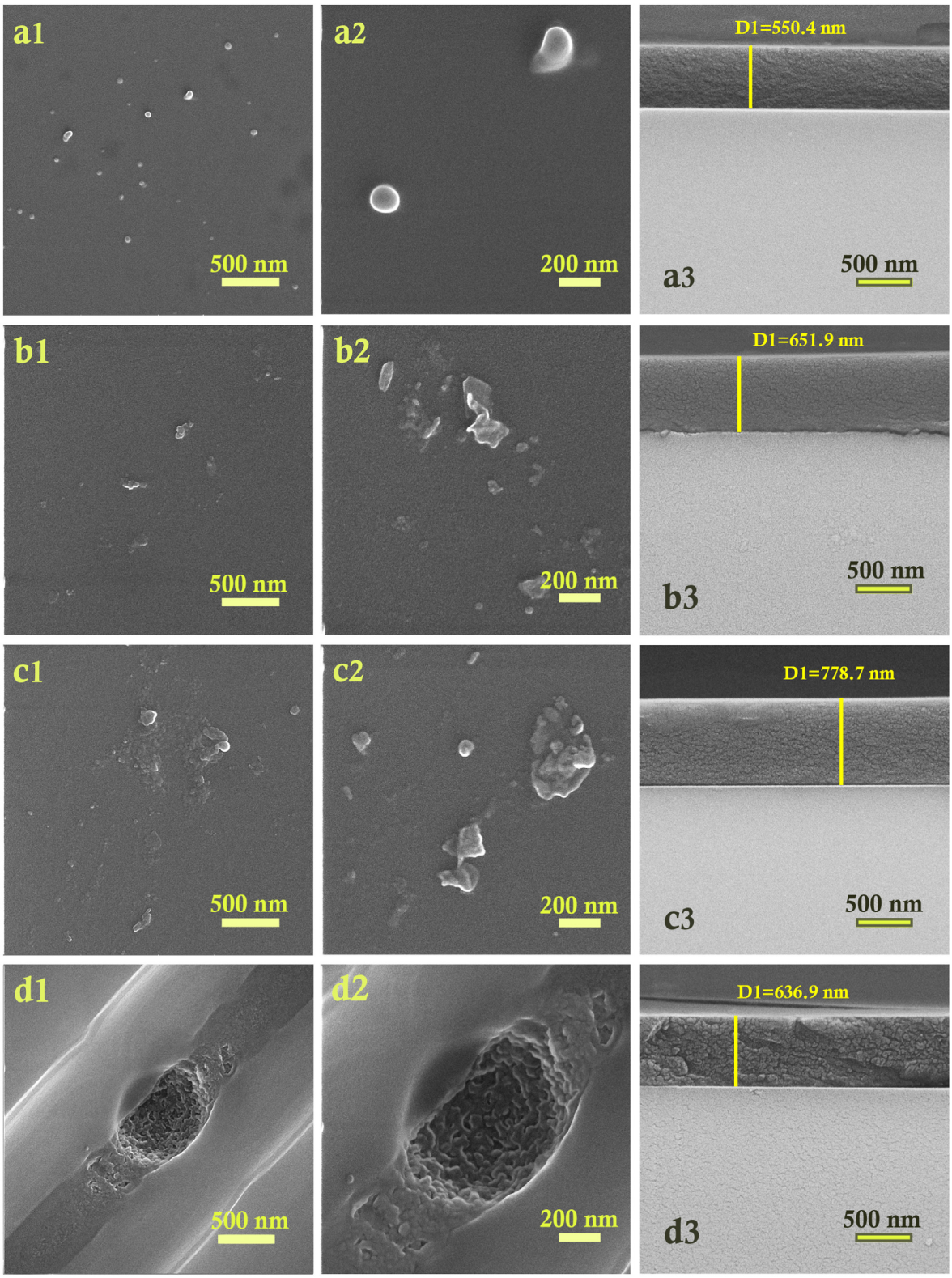

Fig. 9. FEG-SEM images of the a-C:H:N thin films deposited at a) 50%:50%, b) 40%:60%, c) 30%:70%, and d) 20%:80% CH_4:N_2 gas ratio.

J_{pc} of the a-C:H:N electrode deposited at highest nitrogen fraction are 125 mV and 1.03, respectively. It was achieved that nearly reversible electrode reaction can take place on the surface of electrode 20%:80% in comparison with the others. Besides, as can be seen in Fig. 12, the linear relationship between the square root of the scan rates and the redox peak currents in the optimal electrode (i.e., specimen 20%:80%) implies on a typical diffusion-controlled process [8,60].

In order to study the effect of nitrogen incorporation on the nature of electrode processes such as charge transfer resistance and

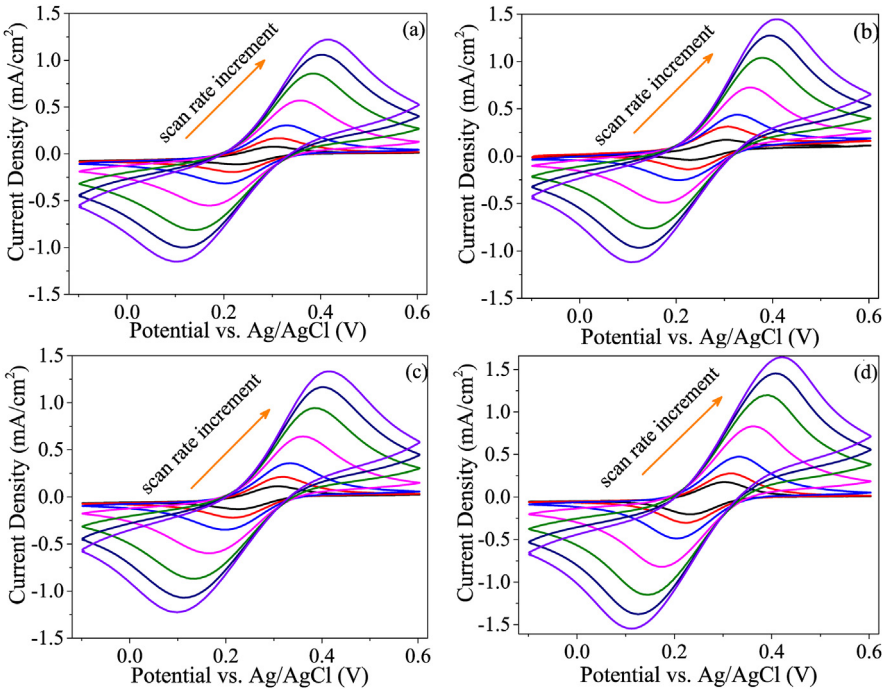

Fig. 10. Cyclic voltammetry curves of a-C:H:N electrodes with different nitrogen concentrations at various scan rates, a) 50%:50%, b) 40%:60%, c) 30%:70%, and d) 20%:80% CH_4:N_2 gas ratio and 5, 10, 20 50, 100, 150, 200 mV/s scan rates.

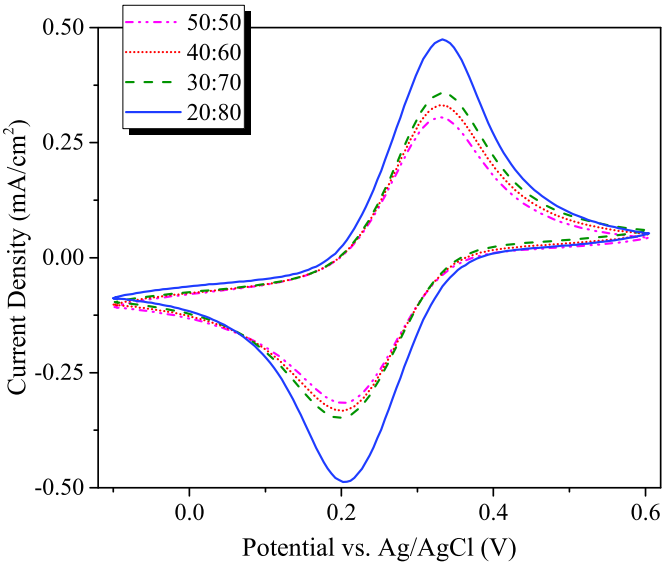

Fig. 11. Comparative CV profiles of a-C:H:N electrodes with different CH_4:N_2 gas ratios at a scan rate of 20 mVs^{-1}.

also the electrochemical properties related to the frequency domain, EIS measurements were conducted for all the a-C:H:N electrodes in the same solution (1 M KCl solution containing 10 mM $K_3Fe(CN)_6$) at open circuit potential. In this regard, Fig. 13 compares the Nyquist plots of a-C:H:N film electrodes in the frequency range of 0.01–10^5 Hz.

Using Randless equivalent circuit shown as the inset to Fig. 13, the empirical impedance spectra were fitted and analyzed, and the pertinent values are summarized in Table 4. The equivalent circuit model includes the electrolyte resistance R_s connected in series with a parallel combination of charge transfer resistance R_{ct} in series with a Warburg impedance W_o and a constant phase element CPE. Instead of the double layer capacitance, the element CPE is employed to characterize the non-ideal action of the capacitance due to the frequency dispersion in this region [12,14,61,62]. Concerning the charge transfer resistance (R_{ct}) values, a similar dependency of the nitrogen incorporation in a-C:H:N electrodes is observed. It was found that the higher nitrogen incorporation in the CH_4:N_2 plasma leads to lower values of the both R_s and R_{ct} and in consequence a faster charge transfer as well as higher electrical conductivity are achieved. Moreover, in the low frequency region, the 20%:80% electrode exhibits a more vertical line than the other electrodes, offering lower mass transfer resistance (Warburg impedance) which expedite ions diffusion [57,62]. These results further confirm the significant electrochemical performance of 20%:80% electrode with the most nitrogen incorporation, which agrees well with findings of the voltammetric data. Furthermore, to specify the apparent heterogeneous charge transfer rate constant k_0, the electrochemical response is employed as follows [12,14,60]:

$$k_0 = \frac{RT}{[C]F^2AR_{ct,\eta=0}} \quad (4)$$

where R, is the molar gas constant (8.314 J K^{-1} mol^{-1}), T, the temperature (298.15 K), [C], the redox species molar concentration, F, the Faraday constant (96,485 $Cmol^{-1}$), A, the geometrical electrode area (10^{-4} m^2), and $R_{ct,\eta=0}$, denotes charge transfer resistance at the zero over potential. The calculated k_0 values are summarized in Table 4. The improvement of k_0 values by increasing nitrogen incorporation highlights the rise of electrode activity due to the increasing presence of N dopants in the a-C:H:N film in accords with the results of CVs.

Besides, the electron rate constants (k_0) measured for N-DLC or a-C:H:N electrodes in this study are 1–3 orders of magnitudes greater than the results found by other deposition techniques in various literatures [6,60,63]. These results revealed that the a-C:H:N thin film electrode with high nitrogen incorporation

Table 4
Electrochemical data of a-C:H:N electrodes with different nitrogen concentration deposited on FTO substrates for the $K_3Fe(CN)_6^{3-/4-}$ redox couple.

CH_4:N_2 gas ratio (%)	ΔE_p (V)	J_{pa}/J_{pc}	R_s (Ω)	R_{ct} (Ω)	CPE (μF/cm^2)	k_0 x10^{-4} (cm s^{-1})
50:50	0.132	1.15	40.46	863	1.31	3.08
40:60	0.132	1.13	24.40	882	1.19	3.02
30:70	0.130	1.12	21.64	502	3.10	5.30
20:80	0.125	1.03	18.23	404	4.08	6.59

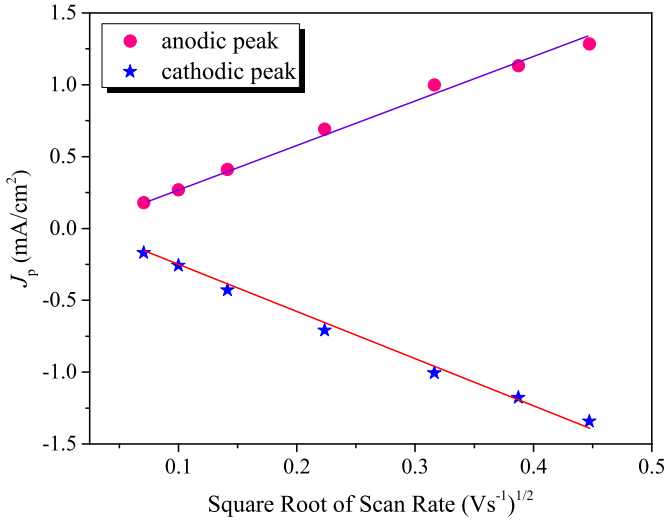

Fig. 12. Dependence of peak current densities of anodic and cathodic reactions on square root of scan rate for a-C:H:N electrode with 20%:80% CH4:N2 gas ratio.

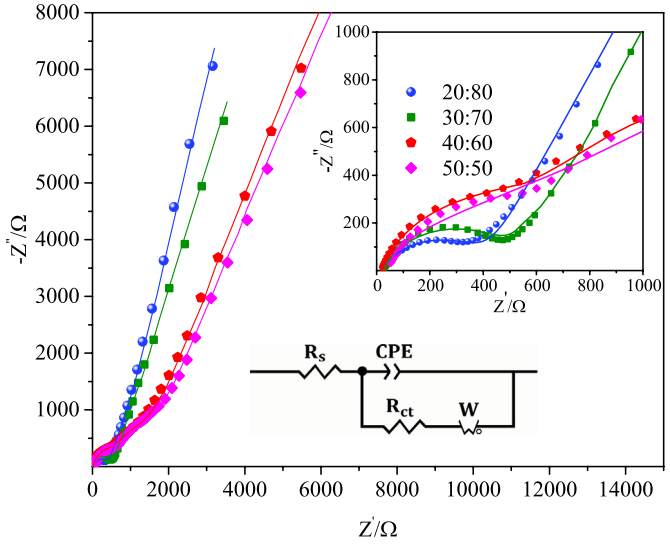

Fig. 13. The EIS Nyquist plots of a-C:H:N thin film electrodes with different nitrogen concentration (The insets are the magnified impedance spectra at high frequency region and the representation of the equivalent circuit of fit).

(especially for the sample 20%:80%) possess an excellent electron transfer ability for redox reaction which exhibits a promising prospect for heavy metal tracing analysis and biosensor applications.

4. Conclusions

In this work, we successfully deposited hydrogenated amorphous carbon-nitride (a-C:H:N, or N-doped DLC) thin films on glass and FTO substrates by a dielectric barrier discharge (DBD) plasma using CH_4/N_2 gas mixture. The effects of nitrogen incorporation on the structural, morphological, optical and electrochemical properties of a-C:H:N thin film were studied by Raman, ATR-FTIR, XPS, FEG-SEM, cyclic voltammetry (CV), and electrochemical impedance spectroscopy (EIS). The experiments were performed at 50%:50%, 40%:60%, 30%:70% and 20%:80% CH_4:N_2 gas ratios. Raman spectra indicated that with increasing the nitrogen incorporation in the films, the size and number of the sp^2 carbon clusters increased. XPS analysis revealed that increasing the nitrogen fraction in the feed gas from 50% to 80% led to an increase of the nitrogen doping content from 5.5 at.% to maximum value 11.5 at.%. Moreover, the influence of the nitrogen incorporation on the structure evolution of samples demonstrated a higher amount of pyridinic N, 6.4 at.%, and graphitic N, 4.7 at.%, in the sample 20%:80% relative to the others. More content of pyridinic and graphitic nitrogen provided more nanopores/active sites as well as excess electrons which led to enhance the electrochemical performance. A decrease in optical band gap from 1.33 eV to 1.09 eV was observed when the nitrogen content (in CH_4:N_2 mixture) increased from 50% to 80%, which resulted in the conductivity enhancement. In addition, in this technique, worm-like porous microstructures were achieved when nitrogen incorporation reached to 80% in CH_4/N_2 mixture. Furthermore, an excellent rate capability and fast redox reactions at electrode/electrolyte interface was observed for 20%:80% electrode in comparison to others. This behavior in the electrode 20%:80% could refer to both the most amounts of active C-N bonds measured by XPS measurements and nanoporous morphology, which led to an enhanced electrochemical performance due to raising the current respond. As a result, good conductivity and high specific surface area which are two desirable factors in reversible electrode reaction and electrochemical response were observed. Moreover, in the low frequency region, the 20%:80% electrode exhibited a more vertical line than the other electrodes, providing lower mass transfer resistance (Warburg impedance) which facilitated ions diffusion. These results further confirmed the significant electrochemical performance of 20%:80% electrode with the most nitrogen incorporation, which agreed well with findings of the voltammetric data. Thus, the 20%:80% a-C:H:N thin film electrode with high nitrogen incorporation, large surface area, abundant holes, and high nano-pore volume possessed an excellent electron transfer ability for redox reaction which exhibited a promising prospect for biosensor, heavy metal tracing analysis and electrochemical applications.

CRediT authorship contribution statement

M. Nilkar: Conceptualization, Methodology, Investigation, Writing - original draft. **F.E. Ghodsi:** Supervision, Conceptualization, Methodology, Validation, Writing - review & editing. **S. Jafari:** Methodology, Validation, Writing - review & editing. **D. Thiry:** Validation, Writing - review & editing. **R. Snyders:** Validation, Writing - review & editing.

Declaration of competing interest

The authors declare that they have no known competing financial interests or personal relationships that could have appeared to influence the work reported in this paper.

Acknowledgments

The authors gratefully acknowledge Prof. M. Arvand and employees of electrochemistry laboratory especially Ph.D. student Maryam Farahmand Habibi for cyclic voltammograms measurements, and University of Guilan Research Council for the support of this work.

References

[1] A. Zeng, V.F. Neto, J.J. Gracio, Q.H. Fan, Diamond-like carbon (DLC) films as electrochemical electrodes, Diam. Relat. Mater. 43 (2014) 12–22.
[2] B. Khadro, et al., Electrochemical performances of B doped and undoped diamond-like carbon (DLC) films deposited by femtosecond pulsed laser ablation for heavy metal detection using square wave anodic stripping voltammetric (SWASV) technique, Sensor. Actuator. B Chem. 155 (2011) 120–125.
[3] O. Chailapakul, W. Siangproh, D.A. Tryk, Boron-doped diamond-based sensors: a review, Sens. Lett. 4 (2006) 99–119.
[4] S.A. Hevia, et. al, Nanometric thin films of non-doped diamond-like carbon grown on n-type (P-doped) silicon substrates as electrochemical electrodes, J. Solid State Electrochem. 22 (2018) 2845–2853.
[5] N. Triroj, R. Saensak, S. Porntheeraphat, B. Paosawatyanyong, V. Amornkitbamrung, Diamond-like carbon thin film electrodes for microfluidic bioelectrochemical sensing platforms, Anal. Chem. 92 (2020) 3650–3657.
[6] Y. Tanaka, et al., Electrochemical properties of N-doped hydrogenated amorphous carbon films fabricated by plasma-enhanced chemical vapor deposition methods, Electrochim. Acta 56 (2011) 1172–1181.
[7] D. Luo, L. Wu, J. Zhi, Fabrication of boron-doped diamond nanorod forest electrodes and their application in nonenzymatic amperometric glucose biosensing, ACS Nano 3 (2009) 2121–2128.
[8] K. Zhou, P. Ke, X. Li, Y. Zou, A. Wang, Microstructure and electrochemical properties of nitrogen-doped DLC films deposited by PECVD technique, Appl. Surf. Sci. 329 (2015) 281–286.
[9] C. Zeng, et al., Enhancement of mechanical, tribological and morphological properties of nitrogenated diamond-like carbon films by gradient nitrogen doping, Diam. Relat. Mater. 76 (2017) 132–140.
[10] W. Guo, et al., Growth of highly nitrogen-doped amorphous carbon for lithium-ion battery anode, Electrochim. Acta 188 (2016) 414–420.
[11] B. Zhang, Y. Yu, Z. Wang, J. Zhang, Structure evolution from nanocolumns to nanoporous of nitrogen doped amorphous carbon films deposited by magnetron sputtering, Appl. Surf. Sci. 256 (2010) 6506–6511.
[12] A. Benchikh, et al., Influence of electrochemical pre-treatment on highly reactive carbon nitride thin films deposited on stainless steel for electrochemical applications, Electrochim. Acta 75 (2012) 131–138.
[13] C.W. Liu, W.E. Chen, Y.T.A. Sun, C.R. Lin, Fabrication and electrochemistry characteristics of nickel-doped diamond-like carbon film toward applications in non-enzymatic glucose detection, Appl. Surf. Sci. 436 (2018) 967–973.
[14] M. Faure, et al., Improvement of electrochemical detection of transthyretin synthetic peptide and its amino acids on carbon electrodes: glassy carbon versus amorphous carbon nitride a-CNx, Electrochim. Acta 296 (2019) 251–258.
[15] W.S. Choi, K. Kim, J. Yi, B. Hong, Diamond-like carbon protective antireflection coating for Si solar cell, Mater. Lett. 62 (2008) 577–580.
[16] T. Cui, et al., Synthesis of nitrogen-doped carbon thin films and their applications in solar cells, Carbon N. Y. 49 (2011) 5022–5028.
[17] R.K. Ghadai, S. Das, S.C. Mondal, B.P. Swain, Investigation of structural and electronic environments of nitrogen-doped CVD-grown DLC films, in: Adv. Electron. Commun. Comput., Springer, 2018, pp. 301–306.
[18] H. Chen, et al., Forming-free resistive switching in a nanoporous nitrogen-doped carbon thin film with ready-made metal nanofilaments, Carbon N. Y. 76 (2014) 459–463.
[19] N. Menegazzo, M. Kahn, R. Berghauser, W. Waldhauser, B. Mizaikoff, Nitrogen-doped diamond-like carbon as optically transparent electrode for infrared attenuated total reflection spectroelectrochemistry, Analyst 136 (2011) 1831–1839.
[20] S.F. Wang, K.K. Rao, T.C.K. Yang, H.P. Wang, Investigation of nitrogen doped diamond like carbon films as counter electrodes in dye sensitized solar cells, J. Alloys Compd. 509 (2011) 1969–1974.
[21] J. Robertson, Plasma deposition of diamond-like carbon, Jpn. J. Appl. Phys. 50 (2011), 01AF01.
[22] L. Ouyang, Z. Cao, H. Wang, R. Hu, M. Zhu, Application of dielectric barrier discharge plasma-assisted milling in energy storage materials—a review, J. Alloys Compd. 691 (2017) 422–435.
[23] F. Khelifa, S. Ershov, Y. Habibi, R. Snyders, P. Dubois, Free-radical-induced grafting from plasma polymer surfaces, Chem. Rev. 116 (2016) 3975–4005.
[24] D. Thiry, S. Konstantinidis, J. Cornil, R. Snyders, Plasma diagnostics for the low-pressure plasma polymerization process: a critical review, Thin Solid Films 606 (2016) 19–44.
[25] R. Rincón, A. Hendaoui, J. De Matos, M. Chaker, Synthesis of flat sticky hydrophobic carbon diamond-like films using atmospheric pressure Ar/CH_4 dielectric barrier discharge, J. Appl. Phys. 119 (2016) 223303.
[26] Y. Hu, L. Li, L. Zhang, Y. Lv, Dielectric barrier discharge plasma-assisted fabrication of g-C3N4-Mn3O4 composite for high-performance cataluminescence H_2S gas sensor, Sensor. Actuator. B Chem. 239 (2017) 1177–1184.
[27] C. Sarra-Bournet, N. Gherardi, H. Glénat, G. Laroche, F. Massines, Effect of C_2H4/N_2 ratio in an atmospheric pressure dielectric barrier discharge on the plasma deposition of hydrogenated amorphous carbon-nitride films (a-C:N:H)„ Plasma Chem. Plasma Process. 30 (2010) 213–239.
[28] C.Y. Su, C.Y. Wu, S.Y. Hsu, C.Y. Wu, J.G. Duh, Improving the electrochemical performance of $LiMn_{0.8}Fe_{0.2}PO_4$ cathode with nitrogen-doped carbon via dielectric barrier discharge plasma, Mater. Lett. (2020) 127880.
[29] J. Niu, L. Zhang, Z. Zhang, D. Liu, Y. Liu, Z. Feng, Deposition of hydrogenated amorphous carbon nitride films by dielectric barrier discharge plasmas, Appl. Surf. Sci. 256 (2010) 6887–6892.
[30] M. Nilkar, F.E. Ghodsi, Effects of annealing atmospheres (Ar, N_2 and air) on structural, morphological, and surface corrosion properties of a-C:H thin films, Diam. Relat. Mater. 98 (2019).
[31] F. Sohbatzadeh, M. Eshghabadi, T. Mohsenpour, Controllable synthesizing DLC nano structures as a super hydrophobic layer on cotton fabric using a low-cost ethanol electrospray-assisted atmospheric plasma jet, Nanotechnology 29 (2018) 265603.
[32] D. Thiry, et al., Toward a better understanding of the influence of the hydrocarbon precursor on the mechanical properties of a-C:H coatings synthesized by a hybrid PECVD/PVD method, plasma process, Polymer 13 (2016) 316–323.
[33] A. Kaniyoor, S. Ramaprabhu, A Raman spectroscopic investigation of graphite oxide derived graphene, AIP Adv. 2 (2012).
[34] A. Ghorbani, A. Sadighzadeh, M. Seifi, S.M. Sadat Kiai, A. Raeisdana, Influence of nitrogen on hydrogenated amorphous carbon thin films deposited by plasma focus device, J. Fusion Energy 37 (2018) 95–102.
[35] G. Messina, A. Paoletti, S. Santangelo, A. Tagliaferro, A. Tucciarone, Nature of non-D and non-G bands in Raman spectra of a-C:H(N) films grown by reactive sputtering, J. Appl. Phys. 89 (2001) 1053–1058.
[36] M. Khadem, O.V. Penkov, V.E. Pukha, M.V. Maleyev, D.E. Kim, Ultra-thin nanopatterned wear-protective diamond-like carbon coatings deposited on glass using a C60 ion beam, Carbon N. Y. 80 (2014) 534–543.
[37] J. Robertson, Diamond-like amorphous carbon, Mater. Sci. Eng. R Rep. 37 (2002) 129–281.
[38] M. Couzi, J.L. Bruneel, D. Talaga, L. Bokobza, A multi wavelength Raman scattering study of defective graphitic carbon materials: the first order Raman spectra revisited, Carbon N. Y. 107 (2016) 388–394.
[39] Y. Kawashima, G. Katagiri, Fundamentals, overtones, and combinations in the Raman spectrum of graphite, Phys. Rev. B 52 (1995) 10053–10059.
[40] L.G. Bulusheva, et al., Effect of nitrogen doping on Raman spectra of multi-walled carbon nanotubes, Phys. Status Solidi Basic Res. 245 (2008) 1971–1974.
[41] A. Majumdar, S.C. Das, T. Shripathi, R. Hippler, Chemical synthesis and surface morphology of amorphous hydrogenated carbon nitride film deposited by N_2/CH_4 dielectric barrier discharge plasma, Compos. Interfac. 19 (2012) 161–170.
[42] U. Martens, H.C. Thejaswini, A. Majumdar, R. Hippler, Deposition of amorphous hydrogenated carbon nitride films with a dielectric barrier discharge, Plasma Process. Polym. 9 (2012) 647–651.
[43] M. Lejeune, F. Brétagnol, G. Ceccone, P. Colpo, F. Rossi, Microstructural evolution of allylamine polymerized plasma films, Surf. Coating. Technol. 200 (2006) 5902–5907.
[44] J. Bian, et al., Thermal vapor condensation of uniform graphitic carbon nitride films with remarkable photocurrent density for photoelectrochemical applications, Nanomater. Energy 15 (2015) 353–361.
[45] D. Thiry, et al., Tailoring the chemistry and the nano-architecture of organic thin films using cold plasma processes, Plasma Process. Polym. 14 (2017) 1700042.
[46] P. Paredez, M.E.H.M. da Costa, L.F. Zagonel, C.T.M. Ribeiro, F. Alvarez, Growth of nitrogenated fullerene-like carbon on Ni islands by ion beam sputtering, Carbon N. Y. 45 (2007) 2678–2684.
[47] R. Swanepoel, Determination of the thickness and optical constants of amorphous silicon, J. Phys. E 16 (1983) 1214.
[48] Z. Seker, H. Ozdamar, M. Esen, R. Esen, H. Kavak, The effect of nitrogen incorporation in DLC films deposited by ECR Microwave Plasma CVD, Appl. Surf. Sci. 314 (2014) 46–51.
[49] N. Dwivedi, et al., Correlation of sp^3 and sp^2 fraction of carbon with electrical, optical and nano-mechanical properties of argon-diluted diamond-like carbon films, Appl. Surf. Sci. 257 (2011) 6804–6810.
[50] Z. Bazhan, F.E. Ghodsi, J. Mazloom, Surface morphology, optical, and electrochromic properties of nanostructured nickel ferrite ($NiFe_2O_4$) prepared by sol–gel method: effects of Ni/Fe molar ratios, Appl. Phys. Mater. Sci. Process 122 (2016).

[51] C. Oppedisano, A. Tagliaferro, Relationship between sp^2 carbon content and E_{04} optical gap in amorphous carbon-based materials, Appl. Phys. Lett. 75 (1999) 3650–3652.
[52] G. Carotenuto, et al., all, Mechanical properties of low-density polyethylene filled by graphite nanoplatelets, Nanotechnology 23 (2012).
[53] J. Wang, et al., Synthesis of carbon nanosheets by inductively coupled radio-frequency plasma enhanced chemical vapor deposition, Carbon N. Y. 42 (2004) 2867–2872.
[54] Z. Bo, et al., Understanding growth of carbon nanowalls at atmospheric pressure using normal glow discharge plasma-enhanced chemical vapor deposition, Carbon N. Y. 49 (2011) 1849–1858.
[55] M. Zhu, et al., Synthesis of carbon nanosheets and carbon nanotubes by radio frequency plasma enhanced chemical vapor deposition, Diam. Relat. Mater. 16 (2007) 196–201.
[56] H. Ling, J.D. Wu, J. Sun, W. Shi, Z.F. Ying, F.M. Li, Electron cyclotron resonance plasma-assisted pulsed laser deposition of boron carbon nitride films, Diam. Relat. Mater. 11 (2002) 1623–1628.
[57] L. Abbasi, M. Arvand, S.E. Moosavifard, Facile template-free synthesis of 3D hierarchical ravine-like interconnected $MnCo_2S_4$ nanosheet arrays for hybrid energy storage device, Carbon N. Y. 161 (2020) 299–308.
[58] Z. Bazhan, F.E. Ghodsi, J. Mazloom, The surface wettability and improved electrochemical performance of nanostructured $CoxFe_{3-x}O_4$ thin film, Surf. Coating. Technol. 309 (2017) 554–562.
[59] M. Layegh, F.E. Ghodsi, H. Hadipour, Experimental and theoretical study of Fe doping as a modifying factor in electrochemical behavior of mixed-phase molybdenum oxide thin films, Appl. Phys. Mater. Sci. Process 126 (2020) 1–14.
[60] N. Liu, et al., A niobium and nitrogen Co-doped DLC film electrode and its electrochemical properties, J. Electrochem. Soc. 164 (2017) H1091–H1098.
[61] M. Layegh, F.E. Ghodsi, H. Hadipour, Improving the electrochemical response of nanostructured MoO_3 electrodes by Co doping: synthesis and characterization, J. Phys. Chem. Solid. 121 (2018) 375–385.
[62] Z. Bazhan, F.E. Ghodsi, J. Mazloom, Modified voltammetric, impedimetric and optical behavior of polymer- assisted sol-gel $MgFe_2O_4$ nanostructured thin films, Electrochim. Acta 250 (2017) 143–151.
[63] P. Tamiasso-Martinhon, H. Cachet, C. Debiemme-Chouvy, C. Deslouis, Thin films of amorphous nitrogenated carbon a-CN_x: electron transfer and surface reactivity, Electrochim. Acta 53 (2008) 5752–5759.